Monthly Notices of the ROYAL ASTRONOMICAL SOCIETY

MNRAS **517,** 1048–1057 (2022) https://doi.org/10.1093/mnras/stac2638
Advance Access publication 2022 September 17

VLT/UVES observation of the SDSS J2357−0048 outflow

Doyee Byun [1]★ Nahum Arav[1] and Patrick B. Hall[2]

[1]*Department of Physics, Virginia Tech, Blacksburg, VA 24061, USA*
[2]*Department of Physics and Astronomy, York University, Toronto, ON M3J 1P3, Canada*

Accepted 2022 September 12. Received 2022 August 17; in original form 2022 April 27

ABSTRACT

We found a broad absorption line (BAL) outflow in the VLT/UVES spectrum of the quasar SDSS J235702.54−004824.0, in which we identified four subcomponents. We measured the column densities of the ions in one of the subcomponents ($v = -1600$ km s^{-1}), which include O I and Fe II. We found the kinetic luminosity of this component to be at most ~ 2.4 per cent of the quasar's Eddington luminosity. This is near the amount required to contribute to active galactic nucleus feedback. We also examined the time variability of a C IV mini-BAL found at $v = -8700$ km s^{-1}, which shows a shallower and narrower absorption feature attached to it in previous SDSS observations from 2000 to 2001, but not in the spectra from 2005 and onwards.

Key words: galaxies: active – quasars: absorption lines – quasars: individual: SDSS J235702.54−004824.0.

1 INTRODUCTION

Quasar outflows are often seen as absorption troughs blueshifted relative to the quasar rest frame in $\lesssim 40$ per cent of quasar spectra (Hewett & Foltz 2003; Dai, Shankar & Sivakoff 2008; Knigge et al. 2008), often invoked as likely producers of active galactic nucleus (AGN) feedback (e.g. Silk & Rees 1998; Scannapieco & Oh 2004; Yuan et al. 2018; Vayner et al. 2021; He et al. 2022). Theoretical estimates require these outflows to have a kinetic luminosity ($\dot{E}_k$) of ~ 0.5 per cent (Hopkins & Elvis 2010) or ~ 5 per cent (Scannapieco & Oh 2004) of the quasar Eddington luminosity ($L_{\rm Edd}$) to significantly contribute to AGN feedback. We have reason to interpret the luminosity mentioned by Hopkins & Elvis (2010) and Scannapieco & Oh (2004) to be $L_{\rm Edd}$ and not the bolometric luminosity ($L_{\rm Bol}$), as explained in section 4 of Miller et al. (2020d). Outflows satisfying these conditions have been found in previous studies (e.g. Moe et al. 2009; Arav et al. 2013, 2020; Chamberlain, Arav & Benn 2015; Leighly et al. 2018; Xu et al. 2019, 2020a, c; Miller et al. 2020a, c; Byun, Arav & Hall 2022).

An outflow's kinetic luminosity depends on its distance from the quasar (R). One way to estimate this distance is by measuring the ionization parameter ($U_{\rm H}$) and electron number density ($n_{\rm e}$) (e.g. Borguet et al. 2012b). Several studies in the past have employed this method to find the distance of outflow systems (e.g. de Kool et al. 2001, 2002a; Hamann et al. 2001; Gabel et al. 2005; Borguet et al. 2012b; Xu et al. 2018; Arav et al. 2020; Miller et al. 2020a, d; Byun et al. 2022). The value of $n_{\rm e}$ can be determined by finding the ratio between the column densities of energy states of the same ion (e.g. Arav et al. 2018).

This paper presents the determination of the R and $n_{\rm e}$ values, along with $\dot{E}_k$, of an outflow system found in the VLT/UVES spectrum of SDSS J235702.54−004824.0 (hereafter J2357−0048). The analysis in this paper has been conducted with data from the VLT/UVES Spectral Quasar Absorption Database (SQUAD) published by Murphy et al. (2019), from which data have been retrieved for a similar analysis of quasar outflows (Byun et al. 2022).

The UVES data of J2357−0048 is from program 075.B-0190(A), and has been added to SQUAD by Murphy et al. (2019) and examined by Chen et al. (2021) for mini-broad absorption line (BAL) systems. Chen et al. (2021) report the presence of four absorption systems, which we independently identified as four sub-components of a BAL outflow. We found the lowest velocity system suitable for our analysis, as it shows troughs of excited states of Fe II, O I, and Si II. We also found a high velocity C IV mini-BAL, of which we report the time variability in comparison with SDSS spectra from different epochs.

This paper is structured as follows. Section 2 discusses the observation and data acquisition of J2357−0048. Section 3 shows the ionic column density measurements and the $n_{\rm e}$ and $U_{\rm H}$. In Section 4, we present the analysis results and the energetics parameters. We also show the time variability analysis of the high velocity mini-BAL. In Section 5, we discuss the results and other features of the quasar's spectrum, and Section 6 summarizes and concludes the paper. For this analysis, we adopted a cosmology of $h = 0.696$, $\Omega_{\rm m} = 0.286$, and $\Omega_\Lambda = 0.714$ (Bennett et al. 2014), and used the PYTHON astronomy package ASTROPY (Astropy Collaboration 2013, 2018) for cosmological calculations.

2 OBSERVATION AND DATA ACQUISITION

The quasar J2357−0048 (J2000: RA = 23:57:02.54, Dec. = −00:48:24.0; $z = 2.998$) was observed with the VLT/UVES on 2005 September 5 as part of the program 075.B-0190(A), with resolution $R \simeq 40\,000$ and wavelength coverage from 3621 to 10 429 Å (Murphy et al. 2019).

Murphy et al. (2019) report a systemic redshift of $z = 2.998$, also reporting values of $z = 2.998$, $z = 3.012$, $z = 3.005$ from the SDSS, NED, and SIMBAD data bases, respectively. We found a discrepancy between these values and the redshifts that we found from the data

★ E-mail: dbyun@vt.edu

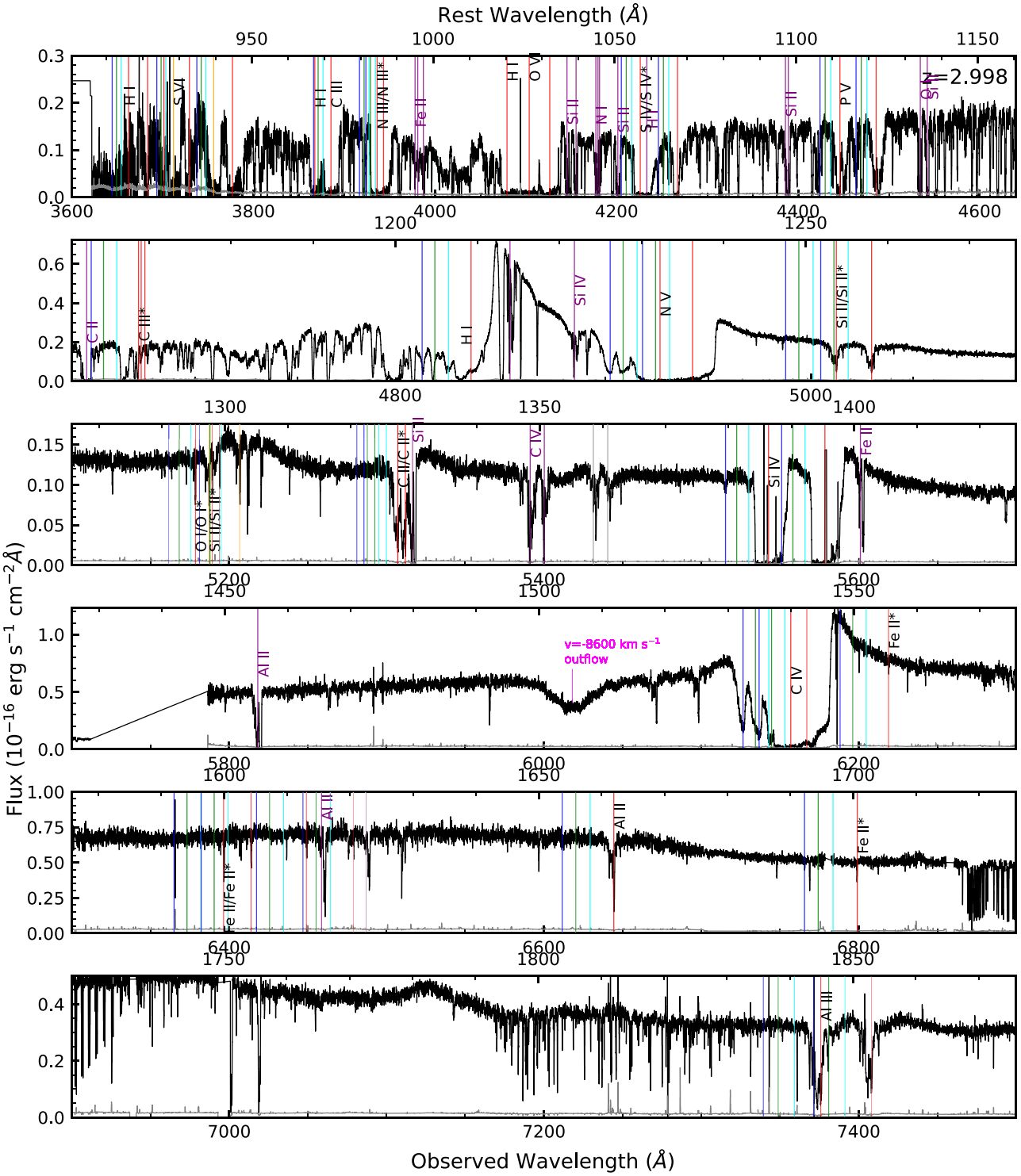

Figure 1. Normalized flux of J2357−0048 multiplied by the emission model by Murphy et al. (2019), based on the SQUAD data set. The flux has been scaled to match the BOSS spectrum from the epoch of MJD = 52203 (2001 October 21) at observed wavelength $\lambda = 6500$ Å. The black curve represents the flux, and the grey shows the error in flux. The red, cyan, green, and blue vertical lines mark absorption troughs of outflow systems S1, S2, S3, and S4, respectively, while the S5 C IV mini-BAL is labelled in magenta. Absorption features of the DLA system are marked in dark purple, and other intervening features are marked in grey. The Si II λλ1304 multiplet of S1 is marked in orange to avoid confusion with the O I multiplet troughs. The S VI doublet of S1 is also marked in orange to avoid confusion with the H I lines. We also marked where the absorption of the C III* multiplet near rest wavelength 1175 Å would be found. Note that we cannot positively identify C III* due to the Lyman-α contamination.

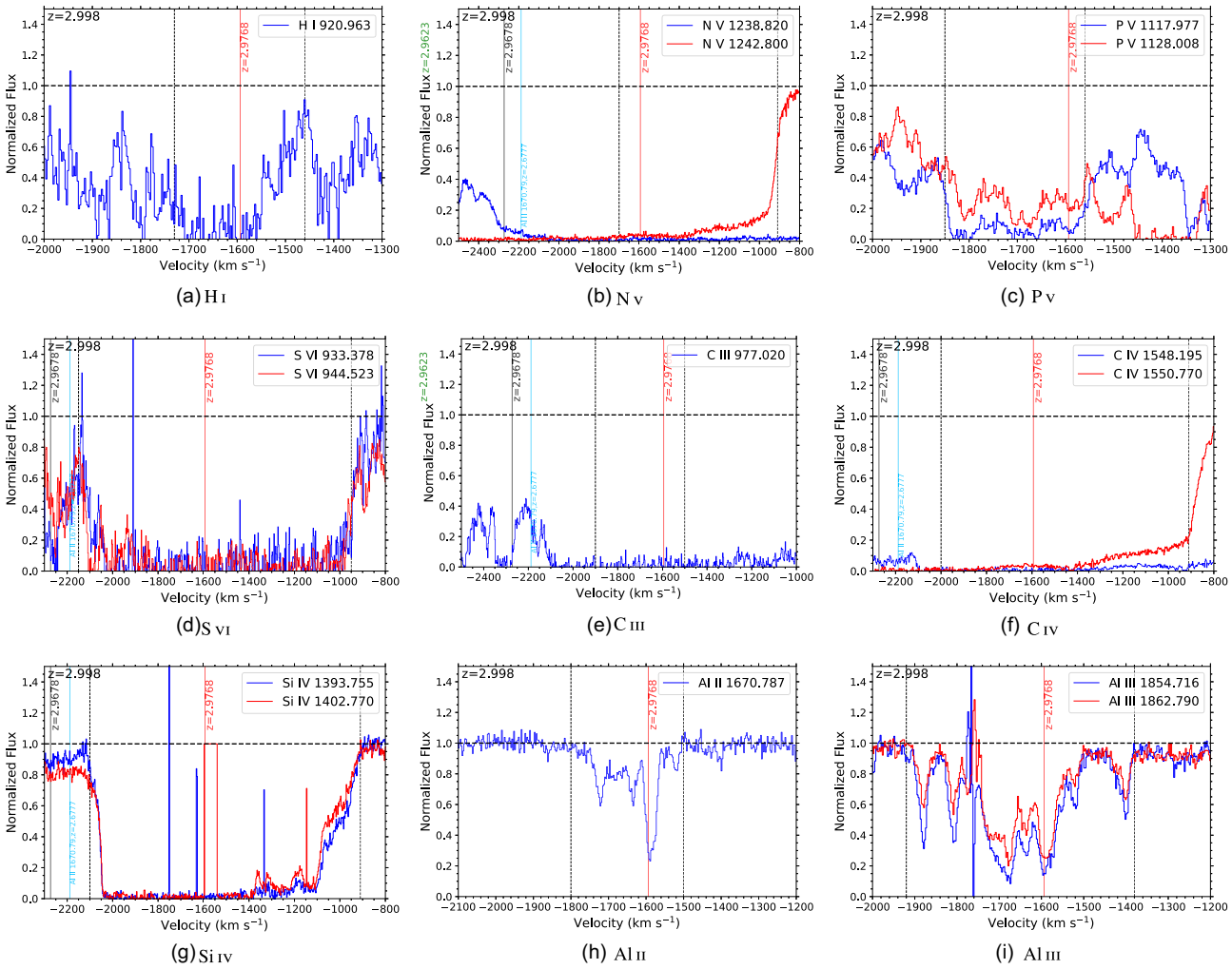

Figure 2. Normalized spectra plotted in velocity space for ions in S1. The velocities of S1 ($z = 2.9768$) and S2 ($z = 2.9678$) are marked with red and black vertical lines, respectively. The dotted vertical lines show the integration ranges used for column density calculations, while the horizontal dashed line marks the continuum level. The light blue vertical lines mark the intervening absorption systems that contaminate the blue spectra.

bases independently. From the SDSS data, we found redshifts ranging from $z = 3.006$ (ninth data release; Ahn et al. 2012) to $z = 3.062$ (13th data release; Albareti et al. 2017). NED reports $z = 3.063$ citing the 13th SDSS data release, while in SIMBAD we found $z = 3.006$ from the ninth data release. While the literature reports a wide range of redshifts, we found that the systemic redshift $z = 2.998$ reported by Murphy et al. (2019) is consistent with the C IV emission redshift $z = 2.97$, blueshifted relative to the systemic redshift, that we found based on the emission from the SDSS spectrum. We have also found a redshift of $z = 2.99$ with the C III emission complex, consistent with the adopted redshift of $z = 2.998$.

Murphy et al. (2019) reduced and normalized the UVES data by its continuum and emission as part of the SQUAD data base. In Fig. 1, we show the normalized spectrum multiplied by the emission model, scaled to match the continuum level at observed wavelength $\lambda = 6500$ Å of the SDSS spectrum at the epoch of MJD = 25503. Zafar, Popping & Péroux (2013) report the detection of a damped Ly α (DLA) system at $z = 2.479$, and Chen et al. (2021) have identified four outflow absorption systems, which we identify here as four subcomponents of a BAL outflow (S1 at $v = -1600$ km s^{-1}, S2 at $v = -2300$ km s^{-1}, S3 at $v = -2700$ km s^{-1}, and S4 at $v = -3100$ km s^{-1}). We also identified a high velocity C IV mini-BAL at $z = 2.8849$, which we call S5 in this paper.

The outflows show absorption of low ionization species such as Si II, Fe II, and O I, and others including S IV, C IV, Si IV, H I, and Al III. The focus of this paper's analysis is on S1, as it displays troughs of excited states of Si II, Fe II, and O I, which allowed us to find its n_e, and by extension, R. We converted the normalized spectrum from wavelength space to velocity space using the quasar's systemic redshift, as shown in the plots of Figs 2 and 3.

For our time variability analysis, we have retrieved SDSS spectra from MJD = 51791, 52203, 55477, 56956, and 57688. We corrected the spectra for galactic reddening and extinction with $E(B - V) = 0.0253$ (Schlafly & Finkbeiner 2011) and the extinction model by Fitzpatrick (1999). The SDSS spectra have resolutions of $R \approx 2000$. More details on the SDSS spectra are in Table 1.

3 ANALYSIS

3.1 Ionic column density

We found the ionic column densities (N_{ion}) of S1 as our first step in finding the physical characteristics of the outflow. We employed

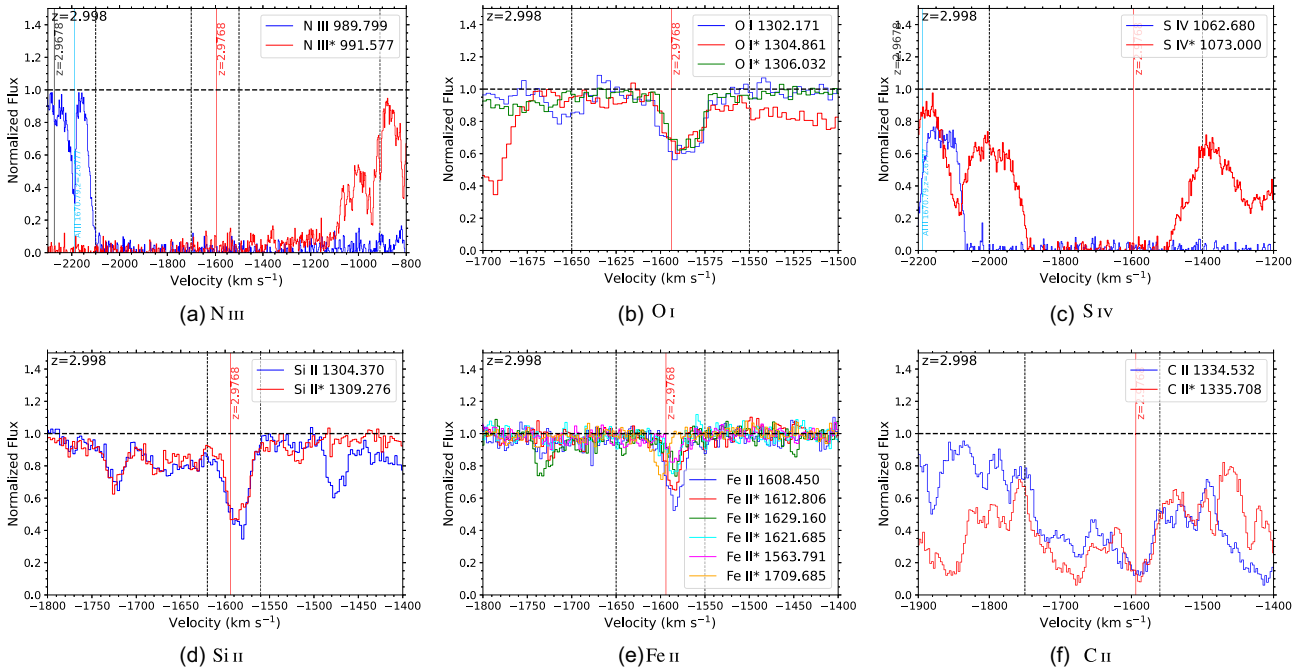

Figure 3. Normalized spectra plotted in velocity space for ions in S1 that display excited states. The format of the plots is the same as in Fig. 2.

Table 1. SDSS spectra information.

MJD	Spectrograph	Plate	Fiber	Observed date	Coverage (Å)
51791	SDSS	387	246	Sep. 4, 2000	3824–9215
52203	SDSS	685	317	Oct. 21, 2001	3820–9202
55477	BOSS	4216	410	Oct. 10, 2010	3565–10 325
56956	BOSS	7850	555	Oct. 26, 2014	3604–10 394
57688	BOSS	9208	969	Oct. 27, 2016	3608–10 334

Table 2. J2357−0048 column densities from UVES observations.

Troughs	Wavelength (Å)	AOD	PC	PL	Adopted	$Z_\odot$-1	$Z_\odot$-2	4.68 $Z_\odot$-1	4.68 $Z_\odot$-2
		S1, $v=-1600$ km s^{-1}							
H I	920.963	$141\,700^{+18\,400}_{-7700}$			$141\,700^{+29\,400}_{-33\,800}$	16.4	3.50	8.0	2.92
N III total		$14\,390^{+830}_{-140}$			$>14\,390_{-2040}$	10.0	1.74	23.87	10.45
N III 0	989.799	7220^{+700}_{-110}							
N III* 174	991.577	7270^{+450}_{-90}							
N V	1238.820 and 1242.800	8640^{+30}_{-30}			$>8640_{-1730}$	1.85	10.41	0.62	2.92
O I total		260^{+7}_{-7}			$>260_{-30}$	0.03	0.75	0.20	0.85
O I 0	1302.171	100^{+4}_{-4}							
O I* 158	1304.861	90^{+4}_{-4}							
O I* 227	1306.032	70^{+4}_{-4}							
P V	1117.977 and 1128.008	677^{+7}_{-6}	740^{+10}_{-10}	510^{+60}_{-10}	510^{+230}_{-100}	0.37	1.10	0.17	0.32
S IV*	1073.000	$14\,330^{+1710}_{-180}$			$>14\,330_{-2870}$	2.67	1.65	3.75	3.44
S VI	933.378 and 944.523	6870^{+360}_{-120}			$>6870_{-1380}$	0.66	1.85	0.39	1.16
C II total		1100^{+10}_{-10}			$>1100_{-220}$	5.27	1.48	11.66	3.18
C II 0	1334.532	490^{+5}_{-5}							
C II* 63	1335.708	610^{+6}_{-6}							
C III	977.020	790^{+100}_{-10}			$>790_{-160}$	815	173	498	293

Table 2 – *continued*

Troughs	Wavelength (Å)	AOD	PC	PL	Adopted	$Z_\odot$-1	$Z_\odot$-2	4.68 $Z_\odot$-1	4.68 $Z_\odot$-2
C IV	1548.195 and 1550.770	8770^{+530}_{-20}			$>8770_{-1750}$	60.1	115	7.01	12.39
Si II total		230^{+4}_{-4}			$>230_{-50}$	4.46	1.03	128	21.04
Si II 0	1304.370	120^{+3}_{-3}							
Si II* 287	1309.276	110^{+3}_{-2}							
Si IV	1393.755 and 1402.770	3320^{+260}_{-20}			$>3320_{-660}$	18.0	3.75	43.2	41.29
Al II	1670.787	$10^{+0.2}_{-0.2}$			$>10_{-2}$	8.3	2.0	51.2	6.16
Al III	1854.716 and 1862.790	$163^{+1.4}_{-1.4}$	218^{+57}_{-3}	391^{+76}_{-3}	390^{+110}_{-170}	1.97	0.22	5.46	2.37
Fe II total		260^{+10}_{-10}			$>260_{-50}$	0.01	0.44	0.40	1.27
Fe II 0	1608.450	60^{+3}_{-3}							
Fe II* 385	1621.685	40^{+5}_{-4}							
Fe II* 668	1629.160	36^{+5}_{-4}							
Fe II* 1873	1612.806	70^{+6}_{-5}							
Fe II* 2430	1563.791	17^{+2}_{-2}							
Fe II* 13474	1709.685	35^{+3}_{-2}							

Note. Column densities have been calculated via numerical integration over $\Delta v = 10\,\mathrm{km\,s^{-1}}$ bins. Energy states of ions are noted with energies in units of $\mathrm{cm^{-1}}$. The wavelengths listed for each ion are the transition rest wavelengths in Å. Most of the adopted values are lower limits due to being AOD measurements. The four rightmost columns show the ratios between modelled and adopted column densities, for the solar one-phase, solar two-phase, supersolar one-phase, and supersolar two-phase solutions, respectively. Units of column density are in $10^{12}\,\mathrm{cm^{-2}}$.

Table 3. Physical Properties of J2357−0048 Outflow. Note that the high-ionization and low-ionization phases of the two-phase solutions are assumed to be co-spatial (at the same distance from the central source). The kinetic luminosity to bolometric luminosity ratios are included for comparison.

Solution	Solar, one-phase	Solar, two-phase		Supersolar, one-phase	Supersolar, two-phase	
Phase	One-phase	Low	High	One-phase	Low	High
$log(N_H)$ [$\mathrm{cm^{-2}}$]	$21.69^{+0.44}_{-0.75}$	$18.96^{+1.05}_{-0.64}$	$21.95^{+1.36}_{-0.72}$	$20.95^{+0.46}_{-0.43}$	$17.96^{+0.93}_{-0.35}$	$20.84^{+0.41}_{-0.30}$
$log(U_H)$ [dex]	$-1.29^{+0.39}_{-0.73}$	$-3.76^{+0.88}_{-0.77}$	$-0.56^{+1.32}_{-0.80}$	$-1.80^{+0.44}_{-0.39}$	$-4.15^{+0.77}_{-0.54}$	$-1.25^{+0.34}_{-0.29}$
$log(n_e)$ [$\mathrm{cm^{-3}}$]	$4.3^{+0.2}_{-0.2}$	$4.3^{+0.2}_{-0.2}$	$1.1^{+1.2}_{-1.5}$	$4.3^{+0.2}_{-0.2}$	$4.3^{+0.2}_{-0.2}$	$1.4^{+0.9}_{-0.7}$
Distance [pc]	640^{+890}_{-260}	$10\,900^{+16\,600}_{-7100}$		1140^{+780}_{-500}	$17\,100^{+16\,600}_{-10\,300}$	
$\dot{M}$ [$\mathrm{M_\odot\ yr^{-1}}$]	14^{+9}_{-8}	$4400^{+30\,700}_{-2270}$		47^{+29}_{-18}	540^{+1190}_{-370}	
$\dot{M}v$ [10^{34} erg s $\mathrm{cm^{-1}}$]	14^{+9}_{-8}	$4400^{+30\,800}_{-2280}$		47^{+29}_{-18}	540^{+1190}_{-370}	
$log(\dot{E}_K)$ [$\mathrm{erg\ s^{-1}}$]	$43.06^{+0.21}_{-0.36}$	$45.55^{+0.90}_{-0.32}$		$43.57^{+0.21}_{-0.21}$	$44.63^{+0.51}_{-0.50}$	
$\dot{E}_K/L_{Edd}$ [per cent]	$0.008^{+0.006}_{-0.004}$	$2.35^{+16.80}_{-1.27}$		$0.025^{+0.019}_{-0.011}$	$0.29^{+0.67}_{-0.20}$	
$\dot{E}_K/L_{Bol}$ [per cent]	$0.006^{+0.004}_{-0.004}$	$1.96^{+13.68}_{-1.02}$		$0.021^{+0.013}_{-0.008}$	$0.24^{+0.53}_{-0.16}$	

Table 4. Modeled C III* column densities of the J2357−0048 outflow, in units of cm^{-2}, along with the ratio between the energy states of $J = 2$ and $J = 0$.

Energy level	Solar, one-phase	Solar, two-phase	Supersolar, one-phase	Supersolar, two-phase
$J = 0$	3.66×10^{13}	9.92×10^{12}	1.25×10^{11}	4.48×10^{9}
$J = 1$	2.96×10^{9}	1.21×10^{6}	1.26×10^{7}	1.81×10^{3}
$J = 2$	5.98×10^{13}	3.14×10^{10}	2.33×10^{11}	2.74×10^{7}
$J = 2/J = 0$	1.63	0.003	1.86	0.006

two different methods in measuring the column densities: assuming the apparent optical depth (AOD) of a uniform outflow covering a homogeneous source (Savage & Sembach 1991); and the partial covering (PC) method assuming a partially covered source (Barlow, Hamann & Sargent 1997; Arav et al. 1999a, b).

While the AOD method is convenient in its simplicity, the PC method can provide us with more accurate measurements of ions with doublets of transition lines, taking into account effects such as non-black saturation (e.g. Edmonds et al. 2011; Borguet et al. 2012a). This is done by finding a velocity dependent covering factor for each ion (de Kool, Korista & Arav 2002b; Arav et al. 2005). A more detailed description of these methods can be found in Byun et al. (2022, section 3.1), which used the same methods to analyse the UVES spectrum of the quasar J024221.87+004912.6. We also used an inhomogeneous power law (PL) covering factor for the P V and Al III doublets to improve column density measurements, as done in previous work (e.g. de Kool et al. 2002b; Borguet et al. 2012a; Xu et al. 2018). We incorporated the difference between the PL and PC values as the lower or upper errors for the adopted column density, depending on whether the PL result was smaller or larger than that from the PC method.

For each ion, we chose an integration range covering a visible absorption feature (see Figs 2 and 3). Some ions, such as N V and C IV, exhibit blending between the red and blue troughs of their doublets (see plots b and f of Fig. 2). To minimize the effects of blending, we selected an integration range that avoids an overlap of the red and blue features, and in this paper report a lower limit of the column density based on the AOD assumption. While we show both ground and excited state troughs of S IV in Fig. 3, since S IV λ1062 is contaminated by the damped Lyman-α trough, we only measured the column density of S IV* λ1073 and thus report a lower limit. While C II absorption is visibly present as seen in Fig. 1, the blending between the excited and resonance troughs, as well as contamination from intervening absorption, made it difficult to isolate the troughs. As such, while we computed a lower limit of the total column density of C II, we have excluded it from the electron number density calculation in Section 3.3.

The column density measurements are shown in Table 2. Note that the high column density of H I comes from a measurement based on the Lyman 9 line, which has a wavelength of λ = 920.963 Å; (see plot a of Fig. 2). The errors in column density have been propagated from the error in normalized flux, binned in $\Delta v = 10$ km s^{-1} wide bins. A conservative 20 per cent error has been added in quadrature to the adopted values used for photoionization analysis to take into account the uncertainty in the modeled continuum (Xu et al. 2018). Note that most of the adopted values are lower limits, as we have used the AOD method for most of the ions in the system. We also took AOD measurements of the visible absorption features of S2–S5. The lower limits of H I column densities of S2–S4, measured from the Lyman-α lines, range between ∼400–500 × 10^{12} cm^{-2}, which is several orders of magnitude smaller than the measured H I column density of S1. The C IV of S5 has a lower limit of N(C IV) > 520 × 10^{12} cm^{-2}.

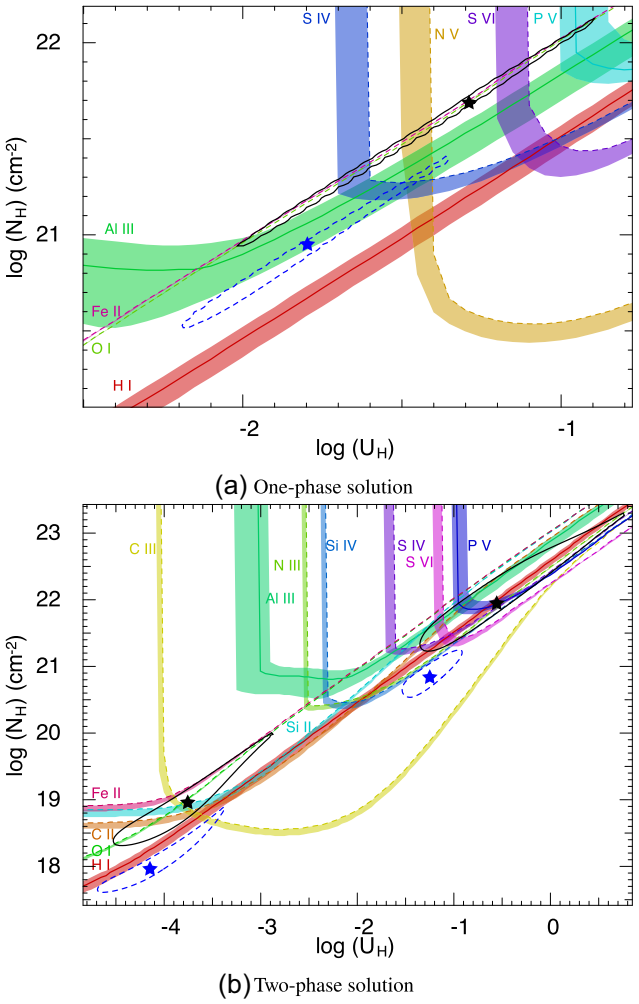

Figure 4. Plot of log N_H versus log U_H for S1. The coloured lines represent the N_H and U_H values allowed by the measured column densities of ions. Solid and dashed lines represent measurements and lower limits, respectively. The coloured bands attached to the lines show the uncertainties in ionic column densities. The black stars and ellipses represent the N_H and U_H solutions, and the 1σ range, assuming solar metallicity. The blue stars and blue dashed ellipses represent the solutions and 1σ range assuming supersolar metallicity ($Z = 4.68\ Z_\odot$; Ballero et al. 2008; Miller et al. 2020b). Note that the lower limits of ions such as C IV and N V are satisfied by any point above their respective coloured bands. The high-ionization phase of the two-phase solution in plot (b) satisfies the lower limits from S IV, S VI, C IV, and N V, making the two-phase solution a better fit to the constraints than the one-phase solution shown in plot (a). The HE0238 SED is assumed.

3.2 Photoionization analysis

We followed the method of previous works to find the ionization parameter (U_H) and the Hydrogen number density (N_H) of the outflow (Xu et al. 2019; Miller et al. 2020a, c; Byun et al. 2022). Using Cloudy (Ferland et al. 2017, version c17.00), we created a grid of photoionization models in order to find the values of N_H and U_H that best fit the ionic column density measurements. Assuming the spectral energy distribution (SED) of quasar HE0238−1904 (hereafter HE0238) (Arav et al. 2013), we created a grid of models

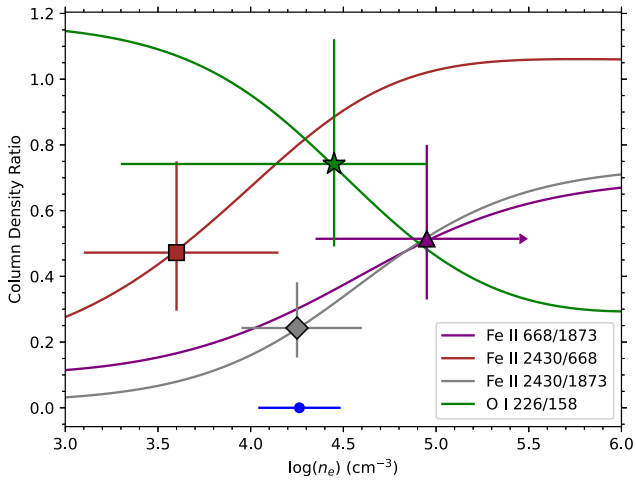

Figure 5. The ratio between the abundances of different energy states of O I and Fe II in S1, assuming a temperature of 10 000 K. The curves represent the theoretical ratios modeled with CHIANTI. The crosses on the curves represent the upper and lower limits of the ratios based on the measured column densities, along with the associated log n_e values. The ratios are colour coded and marked with shapes: Fe II* 668/1873 with a triangle, Fe II* 2430/668 with a square, Fe II* 2430/1873 with a diamond, and O I* 226/158 with a star. The rightward arrow on the purple cross of the Fe II* 668/1873 ratio shows that the data point is a lower limit, as the upper limit of the ratio exceeds the highest point of the curve. The blue dot and error bars show the weighted average of log n_e based on the four measured ratios, which we adopted for our analysis.

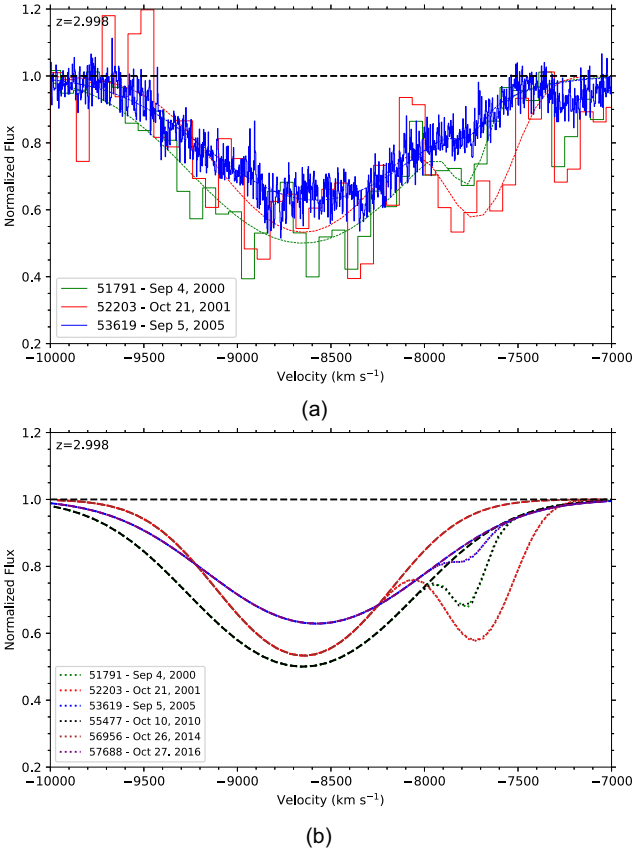

Figure 6. Normalized flux versus velocity of the S5 C IV mini-BAL at three observational epochs. A best fit of two Gaussians was used to model the absorption. (a) shows the models over the data of three epochs, and (b) shows the Gaussians of all six epochs.

with varying values of N_H and U_H. The N_H and U_H values used for each model determine the column density of each ion, which we compared with the measured values in Table 2. A χ^2 analysis has given us the closest matching model to the measurements, as shown in Fig. 4.

We assumed solar metallicity and searched for a one-phase solution (see plot a of Fig. 4), and here report the best-fitting N_H and U_H in Table 3. The solution displays a poor fit to the constraints given by ions such as P V, S VI, and N V. To improve the models' fit with the data, we have calculated one-phase (plot a of Fig. 4) and two-phase (plot b of Fig. 4) solutions with both solar and supersolar ($Z = 4.68\ Z_\odot$; Ballero et al. 2008; Miller et al. 2020b) metallicities, and computed the physical parameters as shown in Table 3. The ratios between modeled and measured column densities can be found in Table 2.

For the two-phase solutions, we attributed the column densities of Fe II and O I to the low-ionization phase, as it was more in line with the constraints given by the measured column densities. The log n_e values (as estimated in Section 3.3) for the high-ionization phase were calculated assuming that the low and high-ionization phases shared the same distance from the central source. Note that the two-phase solutions, both for solar and supersolar metallicity, yield better fits to the column density measurements (see Fig. 4).

3.3 Electron number density

The electron number density (n_e) of the outflow can be found through comparing the column densities of different energy states of ions (e.g. Moe et al. 2009). S1 has absorption troughs of the resonance and excited states of Si II, O I, and Fe II, which we could potentially use for our n_e measurement. We used the CHIANTI 9.0.1 Database (Dere et al. 1997, 2019) for this task, as it models the ratio between energy states dependent on n_e based on collisional excitation.

The Si II ground and excited states display troughs that are nearly identical in depth (see plot d in Fig. 3), suggesting non-black saturation. As it is difficult to find a concrete constraint on the ratio between the two states, we excluded Si II from this process. Finding the ratios between excited and ground states of Fe II and O I gave unphysical values, suggesting saturation of the ground states of Fe II and O I as well. Thus, we found the ratios between excited states instead, as shown in Fig. 5. We then found the weighted mean of the log n_e values from the different ratios, following the linear model method described by Barlow (2003). The resulting value of log n_e can be seen in Table 3.

While we excluded Si II from the process of finding log n_e, we confirmed that the lower limit of the Si II column density was satisfied by the combination of the N_H, U_H, and n_e parameters found by using Cloudy models. The solar one-phase solution estimates log N(Si II) $\approx$ 15.01, while the low ionization phase of the solar two-phase solution predicts log N(Si II) $\approx$ 14.37, both of which are above the lower limit reported in Table 2. While a comparison with an analysis of C III* would have been helpful for additional confirmation of n_e (e.g. Gabel et al. 2005; Borguet et al. 2012b; Arav et al. 2015; Leighly et al. 2018), we were unable to identify the absorption troughs of the C III* 1175 Å multiplet, due to their indistinguishability with the Lyman-alpha forest lines (See Fig. 1). We modeled the column densities of the different energy levels with Cloudy using the N_H, U_H, and n_e values corresponding to each solution (see Table 4).

Table 5. Gaussian fits of C IV mini-BAL at each epoch.

MJD	Date	$\Delta t_{\rm Rest}$ (d)	v_n (km s^{-1})	Δv_n (km s^{-1})	EW_n (km s^{-1})	v_w (km s^{-1})	Δv_w (km s^{-1})	EW_w (km s^{-1})
51791	Sep. 4, 2000	0	-7770 ± 40	0	45	-8650 ± 40	0	690
52203	Oct. 21, 2001	193.9	-7710 ± 50	$+60 \pm 60$	180	-8650 ± 70	0 ± 80	500
53619	Sep. 5, 2005	860.6	-7760 ± 14	-10 ± 40	12	-8577 ± 6	$+70 \pm 40$	515
55477	Oct. 10, 2010	1735.4	-7830 ± 60	-60 ± 70	15	-8650 ± 50	$+0 \pm 70$	500
56956	Oct. 26, 2014	2431.7	-7900 ± 5180	-130 ± 5180	6	-8600 ± 50	$+50 \pm 70$	470
57688	Oct. 27, 2016	2776.3	-7900 ± 200	-10 ± 200	15	-8590 ± 80	$+60 \pm 90$	500

Note. Table of the centroid velocity and equivalent width of the Gaussian profiles fit to the C IV absorption of S5. v_n and v_w are the centroid velocities of the narrow and wide Gaussians. EW_n and EW_w are the equivalent widths of the Gaussians in velocity space. Δv_n, Δv_w, and $\Delta t_{\rm Rest}$ are the changes in velocity and time in the quasar's rest frame from the MJD = 51791 epoch.

The ratio between the $J = 2$ energy state and the $J = 0$ state ranges between 0.003 and 1.86.

4 RESULTS

4.1 Distance and kinetic luminosity of the outflow

The electron number density allows us to find the distance of the outflow from its central source, based on the following definition of the ionization parameter:

$$U_{\rm H} \equiv \frac{Q_{\rm H}}{4\pi R^2 n_{\rm H} c}, \tag{1}$$

where $Q_{\rm H}$ is the rate of Hydrogen ionizing photons, R is the distance of the outflow from the quasar, and $n_{\rm H}$ is the Hydrogen number density. Since $n_{\rm e} \approx 1.2 n_{\rm H}$ for highly ionized plasma (Osterbrock & Ferland 2006), and we found the values of both $U_{\rm H}$ and $n_{\rm e}$ in Section 3 (see Table 3), we could solve the equation for R once the value of $Q_{\rm H}$ was determined.

Following the method of previous works (e.g. Miller et al. 2020a; Byun et al. 2022), we scaled the HE0238 SED to match the continuum flux at rest wavelength $\lambda = 1350$ Å from the SDSS observation on 2001 October 21 ($F_\lambda = 7.27^{+0.82}_{-0.82} \times 10^{-17}$ erg s^{-1} cm^{-2}Å^{-1}), and integrated over the scaled SED for energies above 1 Ryd, finding bolometric luminosity $L_{\rm Bol} = 1.8^{+0.2}_{-0.2} \times 10^{47}$ erg s^{-1} and $Q_{\rm H} = 1.13^{+0.13}_{-0.13} \times 10^{57}$ s^{-1}. The outflow distance calculated from these values is shown in Table 3.

Assuming an outflow with the geometry of an incomplete spherical shell, we calculated the mass flow rate and kinetic luminosity with the following equations (Borguet et al. 2012a):

$$\dot{M} \simeq 4\pi \Omega R N_{\rm H} \mu m_{\rm p} v \tag{2}$$

$$\dot{E}_k \simeq \frac{1}{2} \dot{M} v^2, \tag{3}$$

where Ω is the global covering factor (fraction of the solid angle covered by the outflow), $\mu = 1.4$ is the mean atomic mass per proton, $m_{\rm p}$ is the proton mass, and v is the outflow velocity. We assumed $\Omega = 0.2$, which is the portion of quasars from which C IV BALs are detected (Hewett & Foltz 2003). Calculating the kinetic luminosity yielded values ranging from $\log \dot{E}_K = 43.06^{+0.21}_{-0.36}$ [erg s^{-1}] for the one-phase solution assuming solar metallicity, to $\log \dot{E}_K = 45.55^{+0.90}_{-0.32}$ [erg s^{-1}] for the two-phase solution assuming solar metallicity. Results based on the other solutions can be found in Table 3.

4.2 Changes in the high velocity mini-BAL trough (S5)

We examined the time-variability of the C IV mini-BAL of S5. We adopted the method of Byun et al. (2022), fitting two Gaussian profiles, one broad and one narrow, with the absorption. We added a constraint to the centroid velocity of the narrow Gaussian (-7900 km s^{-1} $< v_c <$ -7600 km s^{-1}), as there was a distinct absorption feature found at $v \approx -7800$ km s^{-1}. As shown in Fig. 6, the smaller absorption feature grows between the observations in 2000 and 2001, but nearly vanishes by 2005. The larger feature becomes gradually shallower. More information of the Gaussian fits can be found in Table 5.

5 DISCUSSION

5.1 AGN feedback contribution of the outflow

The kinetic luminosity ($\dot{E}_K$) of the outflow must be at least $\sim$ 0.5 per cent (Hopkins & Elvis 2010) or $\sim$ 5 per cent (Scannapieco & Oh 2004) of the quasar's Eddington luminosity ($L_{\rm Edd}$) to be a significant contributor to AGN feedback. To find the ratio, we first found the mass and the Eddington luminosity of the quasar. Following the method demonstrated by Vestergaard & Peterson (2006), we computed the mass of the black hole based on the FWHM of the C IV emission in the SDSS spectrum. To account for the blueshift of C IV, we adopted the correction method by Coatman et al. (2017). This yields a mass of $M_{\rm BH} = 1.16^{+0.40}_{-0.30} \times 10^9$ M$_\odot$, corresponding to an Eddington luminosity of $L_{\rm Edd} = 1.5^{+0.5}_{-0.4} \times 10^{47}$ erg s^{-1}. Our one-phase solutions yield $\dot{E}_K/L_{\rm Edd} = 0.008^{+0.006}_{-0.004}$ per cent for solar metallicity and $\dot{E}_K/L_{\rm Edd} = 0.025^{+0.019}_{-0.011}$ per cent for supersolar metallicity, while the two-phase solutions yield $\dot{E}_K/L_{\rm Edd} = 2.35^{+16.80}_{-1.27}$ per cent for solar metallicity and $\dot{E}_K/L_{\rm Edd} = 0.29^{+0.67}_{-0.20}$ per cent for supersolar metallicity (see Table 3). All but the two-phase solar metallicity solution are insufficient to contribute to AGN feedback. The 2.35 per cent ratio from the two-phase solar metallicity solution is above the $\sim$ 0.5 per cent cutoff by Hopkins & Elvis (2010). This is in contrast with the outflow of SDSS J024221.87+004912.6, another SQUAD quasar analyzed by Byun et al. (2022), which exceeded 5 per cent of the quasar's Eddington luminosity. Other quasar absorption outflows in the literature have $\dot{E}_k/L_{\rm Edd}$ values ranging from 0.001 per cent (Chamberlain & Arav 2015) to an upwards of $\sim$ 10 per cent (Chamberlain et al. 2015). A larger sample size of analysed objects may be needed for a statistical analysis.

5.2 The time variability of S5

The most notable change in S5 over time has been of the width and depth of the narrow feature at $v = -7800$ km s^{-1}, which disappeared in the spectrum of 2005 September. The variability of the broader feature afterwards has been minimal, with the equivalent width staying at $\sim$500 km s^{-1}.

One possible explanation for the variability is that there has been a change in photoionization over the different epochs, affecting the depth of the narrow subcomponent (e.g. Xu et al. 2020b; Byun et al. 2022). While other works involve the acceleration of outflow systems due to significant velocity shifts (e.g. Grier et al. 2016), the velocity changes in S5 have been minimal, mostly staying within the margin of error through each epoch.

6 SUMMARY AND CONCLUSION

From the VLT/UVES spectrum of the quasar SDSS J2357–0048, we have identified a BAL outflow with four subcomponents, S1, S2, S3, and S4, as well as a high-velocity C IV mini-BAL, which we label as S5. This paper has presented the analysis of S1, based on the column densities of 14 ions shown in Table 2. We have found estimates of $N_{\rm H}$ and $U_{\rm H}$ through photoionization analysis.

We used the abundance ratios between different energy states of O I and Fe II to find the electron number density $n_{\rm e}$ of S1, as shown in Fig. 5. We have also found other physical parameters of S1 such as distance from the quasar, mass flow rate, and kinetic luminosity, using equations (1), (2), and (3). Based on the ratio between the kinetic luminosity $\dot{E}_k$ and the Eddington luminosity $L_{\rm Edd}$ (see Table 3), the outflow's ability to contribute to AGN feedback has been found to be dependent on the model.

We also examined the time variability of the S5 C IV mini-BAL, based on the SDSS and UVES spectra (see Fig. 6). The small absorption feature at $v = -7700$ km s^{-1} became deeper between the 2000 and 2001 epochs, and nearly vanished in the 2005 epoch. The mini-BAL itself appears to have become gradually shallower over time.

ACKNOWLEDGEMENTS

NA and DB acknowledge support from National Science Foundation (NSF) grant AST 2106249, as well as National Aeronautics and Space Administration (NASA) Space Telescope Science Institute (STScI) grants GO 14777, 14242, 14054, 14176, and AR-15786. DB acknowledges support from the Virginia Space Grant Consortium Graduate Research Fellowship Program. We also thank the anonymous referee for their constructive comments that helped improve this paper.

DATA AVAILABILITY

The normalized UVES spectrum of J2357−0048 is part of the SQUAD data base made available by Murphy (2018) and described by Murphy et al. (2019). The SDSS spectra used for the time variability analysis can be found in the SDSS archive (Stoughton et al. 2002; Aihara et al. 2011; Ahn et al. 2012; Albareti et al. 2017).

REFERENCES

Ahn C. P. et al., 2012, ApJS, 203, 21
Aihara H. et al., 2011, ApJS, 193, 29
Albareti F. D. et al., 2017, ApJS, 233, 25
Arav N., Korista K. T., de Kool M., Junkkarinen V. T., Begelman M. C., 1999a, ApJ, 516, 27
Arav N., Becker R. H., Laurent-Muehleisen S. A., Gregg M. D., White R. L., Brotherton M. S., de Kool M., 1999b, ApJ, 524, 566
Arav N., Kaastra J., Kriss G. A., Korista K. T., Gabel J., Proga D., 2005, ApJ, 620, 665
Arav N., Borguet B., Chamberlain C., Edmonds D., Danforth C., 2013, MNRAS, 436, 3286
Arav N. et al., 2015, A&A, 577, A37
Arav N., Liu G., Xu X., Stidham J., Benn C., Chamberlain C., 2018, ApJ, 857, 60
Arav N., Xu X., Miller T., Kriss G. A., Plesha R., 2020, ApJS, 247, 37
Astropy Collaboration, 2013, A&A, 558, A33
Astropy Collaboration, 2018, AJ, 156, 123
Ballero S. K., Matteucci F., Ciotti L., Calura F., Padovani P., 2008, A&A, 478, 335
Barlow R., 2003, in Lyons L., Mount R., Reitmeyer R., eds, Statistical Problems in Particle Physics, Astrophysics, and Cosmology. Stanford Linear Accelerator Center (SLAC) in Menlo Park, CA, USA, p. 250
Barlow T. A., Hamann F., Sargent W. L. W., 1997, in Arav N., Shlosman I., Weymann R. J., eds, ASP Conf. Ser. Vol. 128, Mass Ejection from Active Galactic Nuclei. Astron. Soc. Pac., San Francisco, p. 13
Bennett C. L., Larson D., Weiland J. L., Hinshaw G., 2014, ApJ, 794, 135
Borguet B. C. J., Edmonds D., Arav N., Dunn J., Kriss G. A., 2012a, ApJ, 751, 107
Borguet B. C. J., Edmonds D., Arav N., Benn C., Chamberlain C., 2012b, ApJ, 758, 69
Byun D., Arav N., Hall P. B., 2022, ApJ, 927, 176
Chamberlain C., Arav N., 2015, MNRAS, 454, 675
Chamberlain C., Arav N., Benn C., 2015, MNRAS, 450, 1085
Chen C., Hamann F., Ma B., Murphy M., 2021, ApJ, 907, 84
Coatman L., Hewett P. C., Banerji M., Richards G. T., Hennawi J. F., Prochaska J. X., 2017, MNRAS, 465, 2120
Dai X., Shankar F., Sivakoff G. R., 2008, ApJ, 672, 108
de Kool M., Arav N., Becker R. H., Gregg M. D., White R. L., Laurent-Muehleisen S. A., Price T., Korista K. T., 2001, ApJ, 548, 609
de Kool M., Becker R. H., Gregg M. D., White R. L., Arav N., 2002a, ApJ, 567, 58
de Kool M., Korista K. T., Arav N., 2002b, ApJ, 580, 54
Dere K. P., Landi E., Mason H. E., Monsignori Fossi B. C., Young P. R., 1997, A&AS, 125, 149
Dere K. P., Zanna G. D., Young P. R., Landi E., Sutherland R. S., 2019, ApJS, 241, 22
Edmonds D. et al., 2011, ApJ, 739, 7
Ferland G. J. et al., 2017, Rev. Mex. Astron. Astrofis., 53, 385
Fitzpatrick E. L., 1999, PASP, 111, 63
Gabel J. R. et al., 2005, ApJ, 631, 741
Grier C. J. et al., 2016, ApJ, 824, 130
Hamann F. W., Barlow T. A., Chaffee F. C., Foltz C. B., Weymann R. J., 2001, ApJ, 550, 142
He Z. et al., 2022, Science Advances, 8
Hewett P. C., Foltz C. B., 2003, AJ, 125, 1784
Hopkins P. F., Elvis M., 2010, MNRAS, 401, 7
Knigge C., Scaringi S., Goad M. R., Cottis C. E., 2008, MNRAS, 386, 1426
Leighly K. M., Terndrup D. M., Gallagher S. C., Richards G. T., Dietrich M., 2018, ApJ, 866, 7
Miller T. R., Arav N., Xu X., Kriss G. A., Plesha R. J., 2020a, ApJS, 247, 39
Miller T. R., Arav N., Xu X., Kriss G. A., Plesha R. J., 2020b, ApJS, 247, 41
Miller T. R., Arav N., Xu X., Kriss G. A., Plesha R. J., 2020c, ApJS, 249, 15
Miller T. R., Arav N., Xu X., Kriss G. A., 2020d, MNRAS, 499, 1522
Moe M., Arav N., Bautista M. A., Korista K. T., 2009, ApJ, 706, 525
Murphy M., 2018, MTMurphy77/UVES_SQUAD_DR1: First data release of the UVES Spectral Quasar Absorption Database (SQUAD)
Murphy M. T., Kacprzak G. G., Savorgnan G. A., Carswell R. F., 2019, MNRAS, 482, 3458
Osterbrock D. E., Ferland G. J., 2006, Astrophysics of Gaseous Nebulae and Active Galactic Nuclei. University Science Books, Sausalito, California
Savage B. D., Sembach K. R., 1991, ApJ, 379, 245
Scannapieco E., Oh S. P., 2004, ApJ, 608, 62
Schlafly E. F., Finkbeiner D. P., 2011, ApJ, 737, 103
Silk J., Rees M. J., 1998, A&A, 331, L1
Stoughton C. et al., 2002, AJ, 123, 485

Vayner A. et al., 2021, ApJ, 919, 122
Vestergaard M., Peterson B. M., 2006, ApJ, 641, 689
Xu X., Arav N., Miller T., Benn C., 2018, ApJ, 858, 39
Xu X., Arav N., Miller T., Benn C., 2019, ApJ, 876, 105
Xu X., Arav N., Miller T., Kriss G. A., Plesha R., 2020a, ApJS, 247, 38
Xu X., Arav N., Miller T., Kriss G. A., Plesha R., 2020b, ApJS, 247, 40
Xu X., Arav N., Miller T., Kriss G. A., Plesha R., 2020c, ApJS, 247, 42
Yuan F., Yoon D., Li Y.-P., Gan Z.-M., Ho L. C., Guo F., 2018, ApJ, 857, 121
Zafar T., Popping A., Péroux C., 2013, A&A, 556, A140

This paper has been typeset from a TEX/LATEX file prepared by the author.